Desalination and Water Treatment
www.deswater.com

doi: 10.5004/dwt.2023.30061

313 (2023) 130–141
November

Controllable one-step production of 2D MgAl-LDH for photocatalytic removal of tetracycline

Xinqi Long, Yinke Wang, Jun Hu, Lixu Wu, Chun Sun, Feipeng Jiao*

School of Chemistry and Chemical Engineering, Central South University, Changsha 410083, China, Tel.: +86 0731-8830833; emails: jiaofp@csu.edu.cn (F. Jiao), longxq@csu.edu.cn (X. Long), 1160489359@qq.com (Y. Wang), hujun0122@163.com (J. Hu), 212312129@csu.edu.cn (L. Wu), 212312139@csu.edu.cn (C. Sun)

Received 25 June 2023; Accepted 9 October 2023

ABSTRACT

In this work, 2D MgAl-layered double hydroxide (LDH) nanosheets were prepared by a one-step hydrothermal method with adding H_2O_2. The as-prepared products were characterized by X-ray diffraction, scanning electron microscopy, transmission electron microscopy, energy-dispersive X-ray spectroscopy, Fourier-transform infrared spectroscopy, X-ray photoelectron spectroscopy, UV-Vis diffuse reflectance spectroscopy, and N_2 adsorption–desorption techniques. Particularly, with 30%wt H_2O_2, MA-4 exhibits the optimal optical properties along with the largest surface area of 63.21 m^3/g among the fabricated samples. In addition, the photocatalytic activities of MgAl-LDH nanosheets were also tightly related to the concentration of H_2O_2 that 99.34% tetracycline was degraded by 2D MgAl-LDH(MA-4) within 3 h. A possible photocatalytic mechanism was proposed based on the analysis of energy structure and the result of free radical scavenging experiments. Furthermore, the degradation efficiency of MA-4 still reached 85% in five successive cycles, which showed remarkable reusability and stability. In this study, the 2D MgAl-LDH nanosheets were expected as a promising catalyst for practical water purification and provide new ideas in the field of two-dimensional photocatalysis.

Keywords: Photocatalyst; Hydrothermal method; 2D MgAl-LDH; Tetracycline; Degradation

1. Introduction

In recent years, antibiotics have been widely applied in medicine, aquaculture, and other fields to meet human needs and boost the industrialization process [1]. Whereas the unrestricted use of antibiotics makes the problem of water pollution more complicated and serious [2]. Due to the weakly natural degradation ability of antibiotics, complete degradation without external action is time-consuming [2,3]. Antibiotics can even enter drinking water through the water cycle, thereby endangering human health [2,3]. Therefore, an efficient method of antibiotic pollutant degradation is in urgent need of further research. Nowadays, various technologies have been used to treat antibiotic wastewater, including membrane separation, adsorption, chlorination degradation, biological sludge, and photocatalysis [4–9]. Among them, photocatalysis is powered by clean and continuous solar energy, with high processing efficiency and recyclability, according to the concept of sustainable development [9].

Layered double hydroxides (LDH), as a representative class of anionic layered materials, consist of positively charged brucite-like layers and anions that balance the charge between the layers. LDH can be expressed by the general formula $[M^{2+}_{1-x}M^{3+}_{x}(OH)_2]^{x+}[A^{n-}_{x/n}]\cdot mH_2O$, where M^{2+} and M^{3+} represent the divalent and trivalent cations in the brucite-like layers, respectively. Besides, A^{n-} is an interlayer anion, and the value of x is $M^{3+}/(M^{2+} + M^{3+})$ [10–13].

* Corresponding author.

There are some advantages of LDH, such as low cost and acid and alkali resistance. Therefore, it has been widely studied in the field of photocatalysis [14,15]. Li and Zeng [16] showed that with the addition of Ag, the loading of Ga_2O_3 on MgAl-LDH could improve the reduction ability of CO_2. Besides, Zhao et al. [17] developed a simple method to prepare LDHs containing multiple cations as efficient and stable photocatalysts, while the sample obtained after calcination had the best CH_4 production effect. However, the traditional LDH material has inevitable defects such as the wide band gap and the small specific surface area. In other words, the immutable layered structure limits itself, which renders the adsorption capacity poor, restricting its photocatalytic performance.

Compared with high dimensional materials, most two-dimensional materials have more active sites and higher adsorption capacity. Thus, 2D materials such as MXenes and nanocrystalline ZnO have attracted the attention of many scholars in recent years [18–21]. Fan et al. [18] found that 2D/2D ZnO/rGO, due to its porous structure and large surface area, had better photocatalytic effect. Yang et al. [19] discovered that since oxygen defect type and concentration differed from 3D ZnO, low dimensional ZnO, whose infrared absorption band divided and transformed, had a higher rate of photo-induced carrier delivery and significant increase in the degradation efficiency of methyl orange. Chen et al. [20] summarized that Ti_3C_2 MXenes, a new type of 2D layered material, which could easily be transformed into thin 2D nano-piece material, was not only large in surface area, but also had Schottky junction inhibiting the composite of the photo-induced carrier. Iguchi et al. [21] reviewed that MXenes had also made significant progress in solar energy conversion, which was attributed to the abundance of active sites. Literature search indicates that most current research aimed at improving the catalytic efficiency by loading material on LDH [16,17,22–24]. Although hydrotalcite has been studied for decades, there were few documents involved in stripping layers of LDH.

In this work, using H_2O_2 as a stripping agent, 2D MgAl-LDH series materials were prepared by a one-step hydrothermal method. The as-prepared samples were characterized, whose photocatalytic properties were investigated by the degradation of tetracycline (TC) as a simulated antibiotic pollutant. In addition, the participation degree of the active group was determined by free radical capture experiments, based on which possible mechanism of photocatalysis was discussed.

2. Experimental set-up

2.1. Materials

$Mg(NO_3)_2{\cdot}6H_2O$ was obtained from Shandong West Asia Chemical Industry Co., Ltd., (China). $Al(NO_3)_3{\cdot}9H_2O$ and tetracycline hydrochloride were both purchased from Shanghai Aladdin Biochemical Technology Co., Ltd., (China). Urea was provided by Tianjin Guangfu Science and Technology Development Co., Ltd., (China). 30% H_2O_2 was bought from Yantai Jianshuo Chemical Co., Ltd., (China). All the reagents were of analytical grade and used without any purification. The whole experiments were conducted with deionized water.

2.2. Preparation of 2D MgAl-LDH

Based on previous literature, MgAl-LDH was prepared by hydrothermal method [25,26]. Firstly, 8 mmol $Mg(NO_3)_2{\cdot}6H_2O$, 4 mmol $Al(NO_3)_3{\cdot}9H_2O$, and 40 mmol urea were added into 80 mL of deionized water to make them fully dissolved. The prepared solution was transferred to a 100 mL Tefon-lined autoclave and reacted in a 150°C thermostatic oven for 12 h. Finally, the slurry was centrifuged several times and then put into a 60°C vacuum drying oven to dry overnight. After drying and grinding, the white solid is stored for later use and marked as MA-1.

Instead of deionized water, H_2O_2 solutions with mass fractions of 10%, 15%, and 30% were used as solvents, where $Mg(NO_3)_2{\cdot}6H_2O$, $Al(NO_3)_3{\cdot}9H_2O$ and urea were added. The subsequent processing steps were the same as mentioned earlier, and these samples were respectively referred to as MA-2, MA-3, and MA-4.

2.3. Characterization of photocatalysts

The crystallinity and phase analysis of the four materials were measured by XRD (Bruker D8 Advance X-ray Diffraction, Switzerland, Cu-Kα radiation (1.5406 Å)). The X-ray photoelectron spectroscopy (XPS) measurement was performed by Thermo Scientific K-Alpha spectrometer (United States) with 1,486.6 eV Alkα radiation at 5.0×10^{-7} mbar, which was used to identify the elements present in the nanosheet and the types of chemical bonds. Valence band spectrum was used to analyze the energy at VB. The morphology and microstructure of the materials were analyzed by scanning electron microscopy (SEM; Tescan Mira3 LMU, acceleration voltage of 10 kV) and transmission electron microscopy (TEM; TECBAL G2 20 S-TWIN, Czech Republic, maximum acceleration voltage of 200 kV). The Brunauer–Emmett–Teller specific surface area and pore size distribution of the product were estimated using an N_2 adsorption–desorption analyzer (77.3 K, placed for 6 h, and pretreated at 150°C) at liquid nitrogen temperature (–196°C). UV-Vis DRS spectral detection used a spectrophotometer (Shimadzu 2401 Spectrophotometer, Japan) to detect the response region to the spectrum, which can be served to calculate the band gap width. The Fourier-transform infrared spectroscopy (FT-IR) spectra of as-prepared materials were tested on the Avatar 360 spectrometer of Nicolet Instruments Company in the United States with a detection range of 4,000–500 cm^{-1} to determine the group and vibration characteristics existing in the materials.

2.4. Photocatalytic test

With a mercury lamp of 500 W, the photocatalytic properties of the catalysts were tested by photodegradation of TC. In this work, each sample was dispersed into 15 ppm TC solution, ensuring a catalyst concentration of 0.5 g/L. The reaction system was exposed to light after being stirred at a constant speed in the dark for 20 min to establish an adsorption–desorption equilibrium. During the radiation period, 3.5 mL of suspension was collected every 20 min and then filtered. Based on the Beer–Lambert law, the concentration of TC is proportional to the absorbance. Thus, the absorbance of TC at 357 nm was finally measured by UV-Vis

spectrophotometer (UV-9600), investigating the change of concentration of TC at each sample point [9,18].

3. Result and discussion

3.1. Characterization of photocatalysts

3.1.1. X-ray diffraction

Fig. 1 shows the XRD patterns of four samples. In Fig. 1a the diffraction peaks at 2θ = 11.71°, 23.58°, 35.02°, 35.60°, 39.67°, 47.10°, 60.94°, and 62.35° were observed, corresponding to the crystal faces of (003), (006), (012), (009), (015), (018), (110) and (113), respectively. These diffraction peaks with strong intensity and narrow width were consistent with the typical characteristic peaks of LDHs, proving the well-layered stack and high crystallinity of MA-1 [27,28]. Comparing the patterns of MA-1, MA-2, and MA-3 (Fig. 1a–c), it could be found that the peak heights of (003), (006) and (012) decreased gradually with the increased addition of H_2O_2, suggesting the samples began to extend into a lamellar structure, and the thickness became thinner [28]. It is worth noting that the diffraction peak intensities of MA-4 were the weakest among those of all samples. Furthermore, the peaks appeared earlier, indicating that MA-4 possesses thin thickness and large layer spacing. The diffraction peak corresponding to the crystal plane (110) represented arranging ions on the principal plane [27]. As shown in Fig. 1a–c, the height of the corresponding peak on the crystal plane of (110) increased, which was still much lower than the diffraction peak on the (003) crystal plane. However, Fig. 1d exhibited that the peak height of (003) was comparable to (110), demonstrating the well-grown lamellar structure.

3.1.2. X-ray photoelectron spectroscopy

In order to determine the composition, valence electron form, and surface chemical bond of as-prepared MA-4, the sample was characterized by X-ray photoelectron spectroscopy. As the survey scan spectra, Fig. 2a shows that MA-4 contained C, O, Mg, and Al elements. The element peaks in Fig. 2 were all revised, where the lowest binding energy peak of C 1s was corrected to 284.80 eV. Fig. 2b displays the binding energies of C 1s at 284.80, 286.15, and 288.82 eV, which are responsible for chemical bonds of C–C/C=C, C–O, and O–C=O, respectively [28]. In the O 1s XPS spectrum, two peaks at 532.07 and 530.32 eV could be observed after fitting, attributed to C=O and O–H chemical bonds [32]. The spectra in Fig. 2d and e are unimodal, with peaks at 73.96 and 1,304.05 eV, which were assigned to Al–O and Mg–O [28,29].

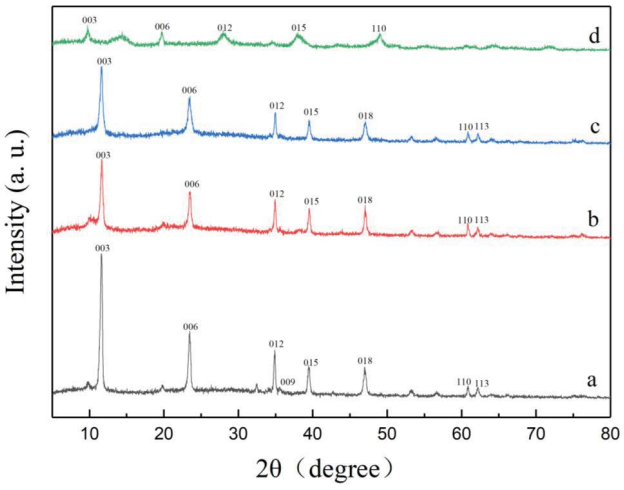

Fig. 1. X-ray diffraction patterns: (a) MA-1, (b) MA-2, (c) MA-3, and (d) MA-4.

3.1.3. Scanning electron microscopy, transmission electron microscopy and energy-dispersive X-ray spectroscopy

As shown in Fig. 3a, under the SEM, MA-1 exhibited obvious stackable layers with aggregation between sheets, which was an emblematic characteristic of hydrotalcite [10,12,27,28]. By comparing Fig. 3b, d and f, it could be seen that the thickness of materials decreased with the increase of the amount of H_2O_2 added in the hydrothermal reaction. In particular, the thickness of MA-1 was about 100 nm, MA-2 was 50 nm and MA-3 was slightly less than 50 nm. However, due to the small thickness of MA-4, it was unclear to observe by SEM images but TEM.

Fig. 3g demonstrates successful large-scale stripped LDH nanosheets. Nevertheless, some ultrathin nanosheets were irregular shapes, even in the form of agglomerations. It is thought to be caused by the addition of 30% H_2O_2, resulting in excessive oxygen generation during the preparation of MA-4. With the high pressure in the reactor, a portion of detached ultrathin nanosheets was compacted [27]. Fig. 3h illustrates the thickness of MA-4 after enhancing magnification, which stated its thickness was smaller than MA-3. The width of the shaded part was about 10–30 nm. Fig. 3i displays the polycrystalline diffraction pattern of MA-4. Digital Micrograph software was used to measure the diameter of the diffraction rings, where 78 length units were 1 nm^{-1}. Searching standard PDF and XRD results for comparison, it revealed that positions of diffraction peaks would appear earlier, thus d (nm^{-1}) in standard value would change. The final values were in good agreement with corresponding values of (003), (006), and (110) crystal plane diffraction peaks, which was considered that the above crystal plane structures existed in MA-4 [30]. The energy-dispersive X-ray spectroscopy (EDS) results of MA-4 are shown in Fig. 3j, proving the existence of Mg, Al, O, and C elements, which was consistent with the result of the XPS full spectrum analysis. According to the proportions in Fig. 3j, the mass ratio and element ratio of O were the highest, while those of C were the lowest. Thus, it can be speculated that the number of CO_3^{2-} filled between layers of LDH decreased, which supported the success of the preparation of 2D MgAl-LDH nanosheets.

3.1.4. Brunauer–Emmett–Teller

The structural parameters of fabricated samples were determined by N_2 adsorption–desorption experiments. Fig. 4 demonstrates N_2 adsorption–desorption isotherms and Barrett–Joyner–Halenda (BJH) pore size distributions of prepared samples. By comparing four isotherms in Fig. 4a,

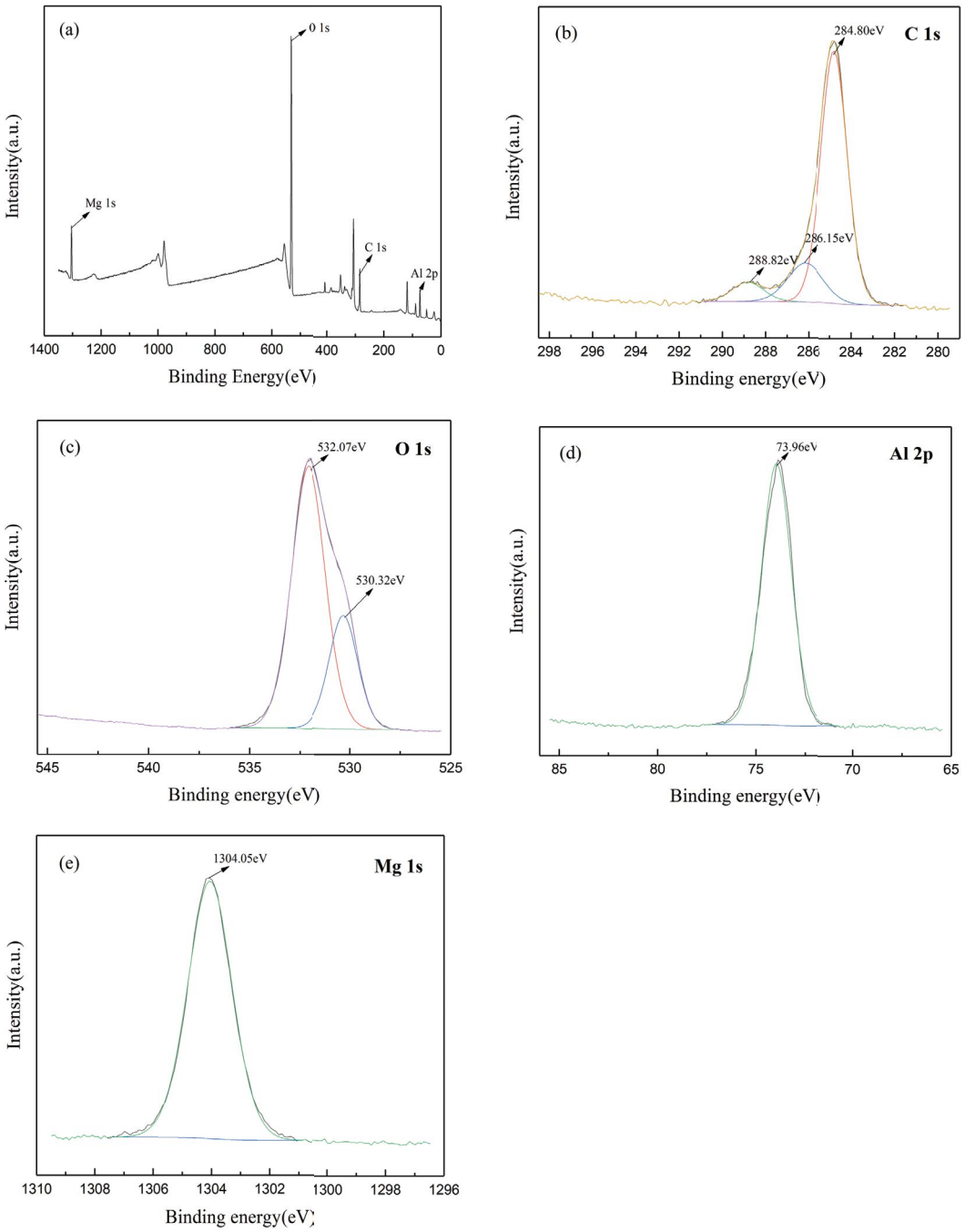

Fig. 2. MA-4 X-ray photoelectron spectra: (a) full spectrum, (b) C 1s spectrum, (c) O 1s spectrum, (d) Al 2p spectrum, and (e) Mg 1s spectrum.

it was found that MA-4 had the highest adsorption capacity, while MA-1 was the lowest. All the curves were determined as typical IV isotherms with H_3 type hysteretic loops, indicating that these catalysts had mesoporous structures [10,12,31]. These results were further proved by the BJH pore size distribution curves in Fig. 4b. All aperture sizes are distributed between 0 and 40 nm.

The specific surface area, pore volume, and average pore diameter of samples are listed in Table 1. Based on the data, with the increase of H_2O_2 addition, the specific surface area and the pore volume enlarged. The specific surface area of MA-4 was more than three times that of MA-1. These results further confirmed the success of stripping, while 2D LDH has a higher area per unit mass than 3D structure. Meanwhile, a higher specific surface area would provide more active sites, which was conducive to photocatalytic reactions. Compared with MA-1, the average pore diameter of other samples with H_2O_2 was slightly increased. It was speculated the O_2 produced by the addition of H_2O_2 made pores larger.

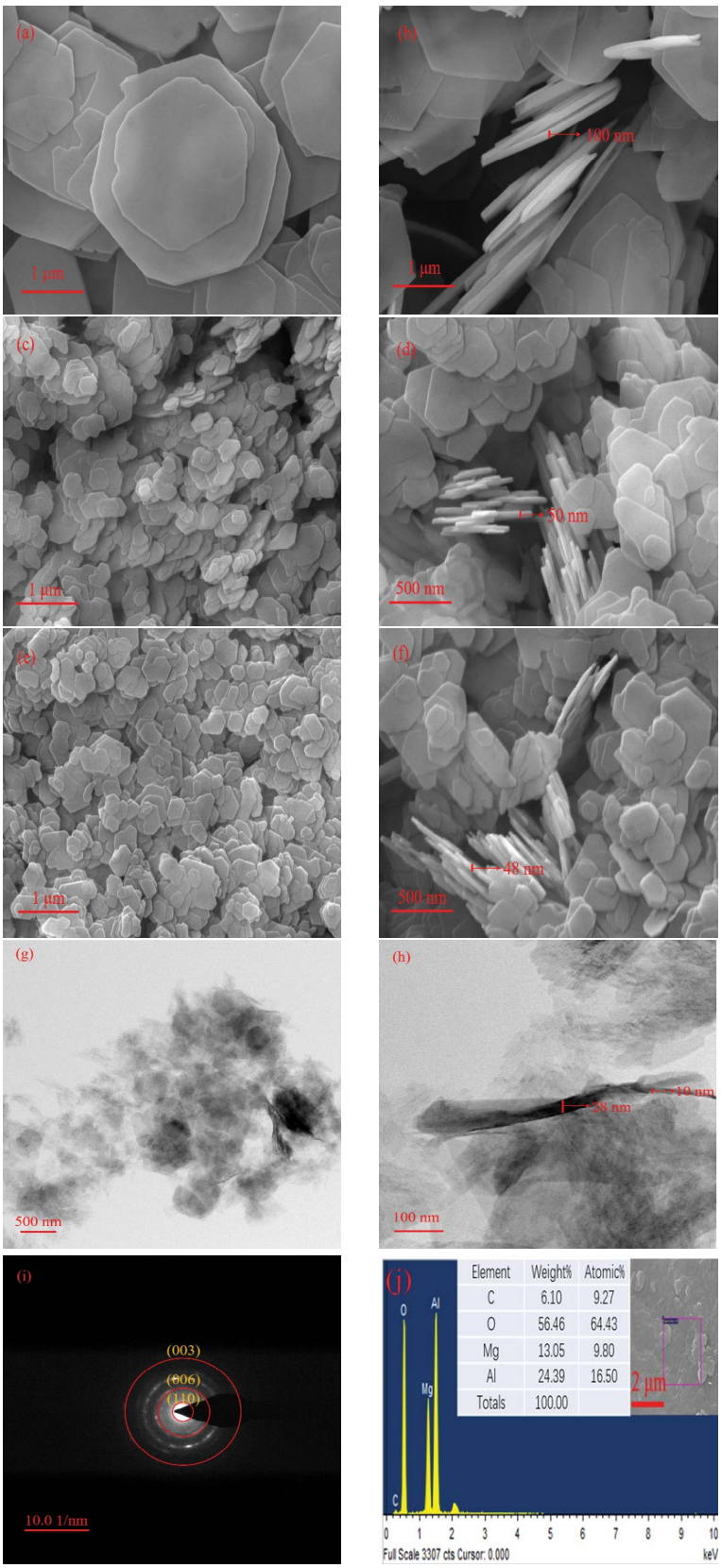

Fig. 3. (a) Positive SEM image of MA-1, (b) SEM profile of MA-1, (c) positive SEM image of MA-2, (d) SEM profile of MA-2, (e) positive SEM image of MA-3, (f) SEM profile of MA-3, (g) positive TEM image of MA-4, (h) TEM profile of MA-4, (i) MA-4 polycrystal diffraction pattern, and (j) MA-4 EDS spectrum.

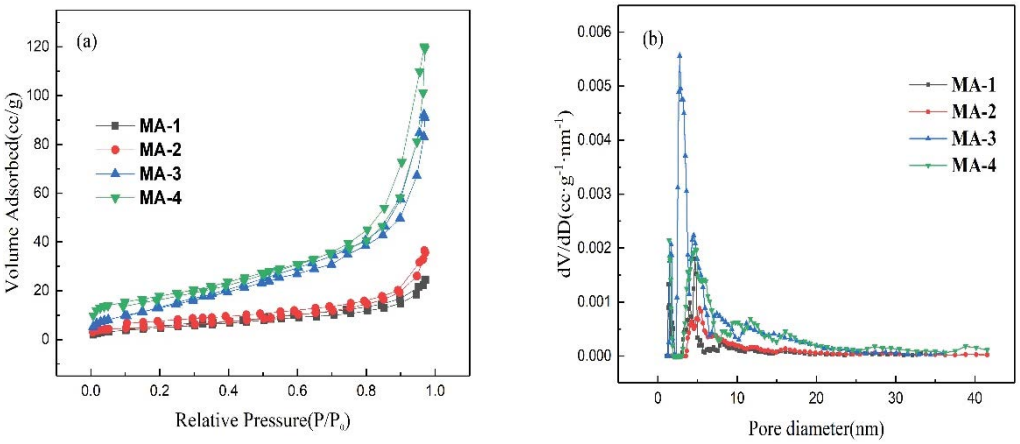

Fig. 4. (a) N_2 adsorption isotherms for MA-1, MA-2, MA-3 and MA-4 and (b) aperture distribution curves.

Table 1
Physical properties of materials

Photocatalyst	Surface area (m^3/g)	Pore volume (cc/g)	Average pore diameter (nm)
MA-1	17.91	0.03794	8.472
MA-2	19.04	0.05516	11.59
MA-3	54.33	0.14080	10.37
MA-4	63.21	0.18420	11.66

3.1.5. UV-Vis DRS

The UV-Vis diffuse reflectance spectra of prepared catalysts are exhibited in Fig. 5a. It was obvious that the light absorbance of these samples was mainly in the ultraviolet region (200–380 nm). Among all the samples, MA-4 not only had the widest light response area but also had the strongest light absorption capacity, especially in the vicinity of a wavelength of 300 nm. The reason was that MA-4 had the largest specific surface area and had more active sites on the surface, which was beneficial to the utilization of light. The original data was processed according to the formula $(Ah\nu) = \alpha(h\nu - E_g)\gamma$. A and α are the absorption coefficient and the tailing parameter. $h\nu$ represents the photon energy. The constant γ is determined by the type of photoelectron transition in the semiconductor. In this work, the value of γ is 2 because the MgAl-LDH is an indirect transition semiconductor material. Thus, the bandgap widths of as-prepared samples could be obtained by Fig. 5b–e [10,32]. By the linear extrapolation at curve mutation, it was found that the bandgap of MA-1, MA-2, MA-3, and MA-4 was 4.20, 4.18, 4.15, and 3.90 eV, respectively. As a result, as the LDH became thinner, the bandgap gradually decreased and the material was easier to be excited by photons.

3.1.6. Fourier-transform infrared spectroscopy

The FT-IR spectra of four as-prepared samples are shown in Fig. 6. The spectrum of each sample showed a strong peak with a center at 3,415.18 cm^{-1}, which was responsible for the tensile vibration of both hydroxyl and hydroxide between layers of hydrotalcite [27,33]. Among all the catalysts, this peak of MA-4 was significantly the broadest. Meanwhile, the sharp peak of MA-4 at 1,058.21 cm^{-1} also belonged to the hydroxyl translational vibration [31]. The bending vibration peak of water was reflected at 1,586.56 cm^{-1}, while the intensity adsorption peak at 1,352.98 cm^{-1} corresponded to the typical vibration mode of ν3 of CO_3^{2-} [28]. The CO_3^{2-} absorption peak of MA-4 was wider, whose height was slightly decreased, indicating that CO_3^{2-} content in MA-4 was slightly reduced. The strong bands at 769.40 and 550.33 cm^{-1} were attributed to M–O stretching and M–OH vibration, respectively [33].

3.1.7. Electrochemical impedance spectroscopy

As depicted in Fig. 7a, compared with pristine MgAl-LDH, MA-4 had the maximum photocurrent density, showing that the MA-4 could effectively strengthen the transfer of photo-generated carriers. In addition, to further realize the characteristics of charge transfer, the electrochemical impedance spectroscopy (EIS) technique was employed. A smaller arc radius means a higher charge carrier transfer efficiency. As displayed in Fig. 7b, the arc radius of MA-4 was the smallest, implying the fastest charge transfer and better separation ability of e^- and h^+.

3.2. Photocatalytic activities of catalysts

3.2.1. Photocatalytic performances for the degradation of TC

In this work, with 15 ppm TC as simulated antibiotic wastewater, photocatalytic properties of four as-prepared samples under light irradiation were explored. After stirring in the dark for 20 min, the equilibrium of adsorption and desorption was established to eliminate the influence of adsorption.

In Fig. 8 the function C/C_0 was the degradation efficiency of catalysts, where C_t and C_0 stood for the concentration at any moment (min) and initial value, respectively [11,17]. After 20 min of dark and 140 min of light, the degradation rate of MA-4 reached 99.34%, showing excellent photocatalytic properties of 2D MgAl-LDH. Under the same

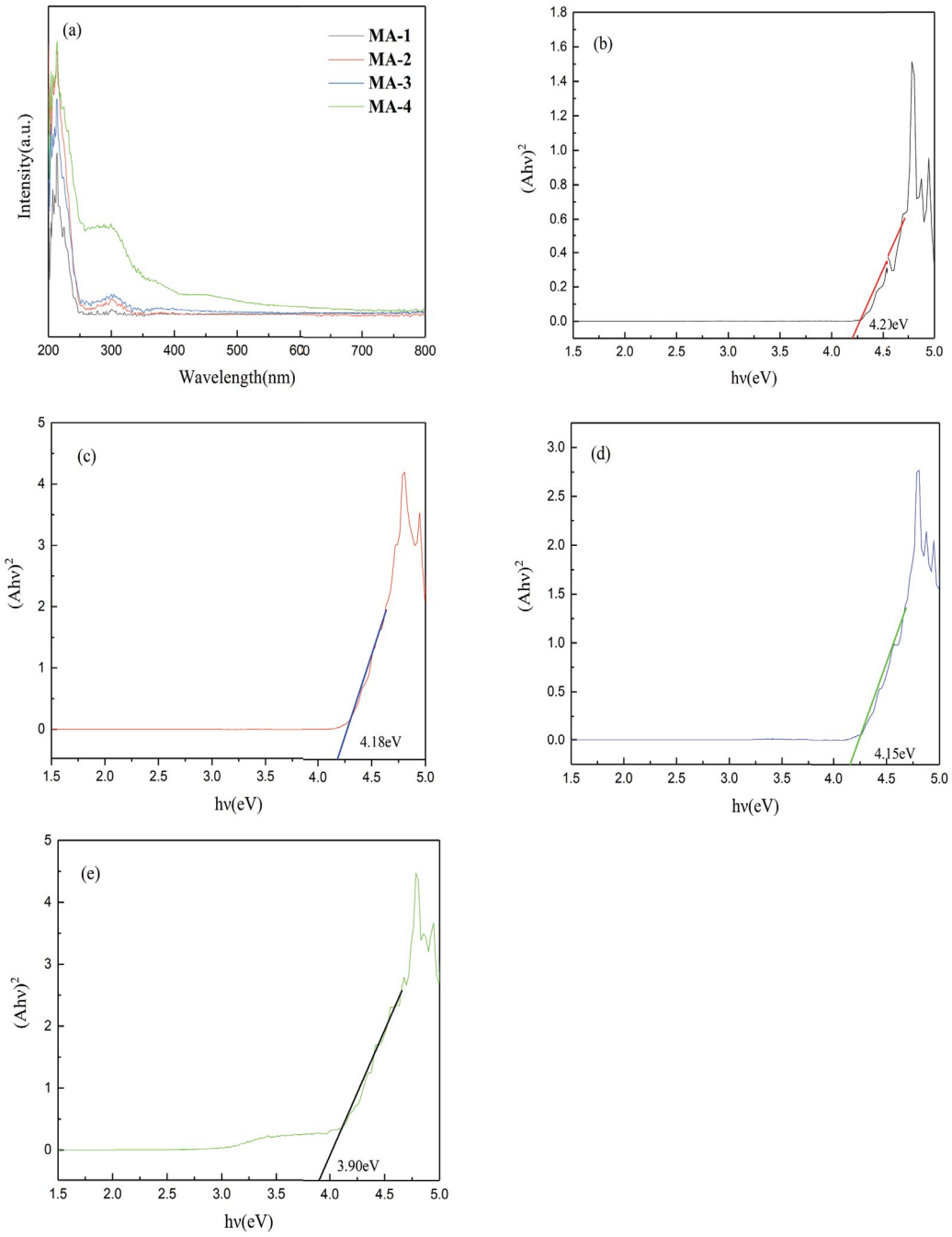

Fig. 5. (a) UV-Vis spectra of MA-1, MA-2, MA-3 and MA-4, (b) forbidden bandwidth of MA-1, (c) forbidden bandwidth of MA-2, (d) forbidden bandwidth of MA-3, and (e) forbidden bandwidth of MA-4.

conditions, the degradation rates of MA-1, MA-2, and MA-3 were 75.77%, 82.91%, and 88.84%, respectively, which were all weaker than MA-4. As Table 2 shows, in comparison with other related materials reported in the literature, MA-4 showed superior degradation properties.

Due to the experimental data and the low TC concentration being matched to the Langmuir–Hinshelwood model, the quasi-first-order kinetics model was used to analyze the degradation process to further evaluate the catalytic activities of those photocatalysts [10,42,43].

$$\ln\left(\frac{C_0}{C_t}\right) = kt \tag{1}$$

where k and t were the pseudo-first-order rated constant (min^{-1}) and time (min). Fig. 8b and c exhibited the kinetics of photocatalytic reaction and apparent reaction constants. After fitting, it was found that the catalytic degradation of TC by MA series materials basically followed the pseudo-first-order kinetic law with great R^2 values. When the

illumination time reached 120 min, about 99% of TC was removed by MA-4. Subsequent data points of low concentration were omitted to eliminate their impact on the fitting curve. Among the four photocatalysts, the apparent reaction rate of MA-4 was the highest at 0.04429 min^{-1}, which was 4.31 times that of MA-1 (0.01027 min^{-1}). As Fig. 8c shows, the order of k values of four samples was MA-4 > MA-3 > MA-2 > MA-1. The reason for this result was that with the addition of H_2O_2 increasing, the 3D MgAl-LDH tended to be two-dimensional. The specific surface area of the catalyst is increased. Therefore, a large number of active sites are fully exposed, and the distance of the photocarrier migration from the interior of the material to the surface is shortened [36,37]. Thus, the photocatalytic activity was enhanced.

3.2.2. Photocatalytic stability of catalysts

As a significant property of the catalyst, the stability was investigated by a cycle test. Therefore, MA-4, with the optimal photocatalytic performance, was selected to carry out the cycle performance experiments. The photocatalytic stability of MA-4 was studied by degrading 15 ppm TC solution repeatedly. During the process of each run, the catalyst concentration was ensured to be 0.5 g/L. After the last round of photodegradation, the catalyst was filtered and fully dried before being put into the next [11].

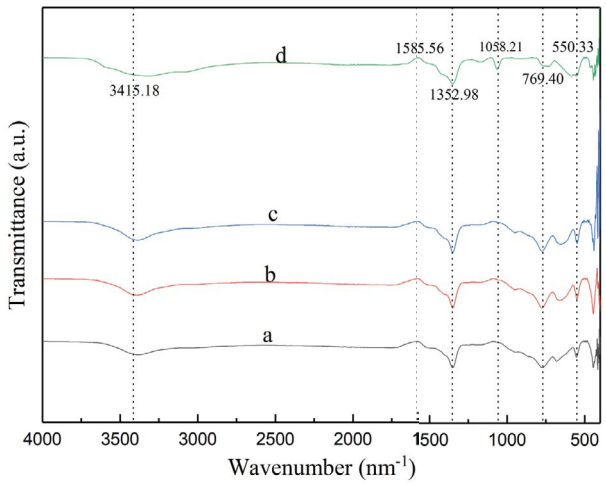

Fig. 6. FT-IR spectra: (a) MA-1, (b) MA-2, (c) MA-3, and (d) MA-4.

As shown in Fig. 9, both the adsorption and photocatalytic capacity of MA-4 decreased after five cycles. The final degradation rates were 98.98%, 98.00%, 95.41%, 89.83%, and 86.93% in five experiments, respectively. The result indicated that in the process of multiple cycle experiments, the photo-corrosion phenomenon of a small amount of MA-4 appeared, resulting in a downward trend of degradation ability after runs. Despite the decrease in performance, the degradation efficiency in the fifth cycle was still 87.82% of the first. Therefore, MA-4 had excellent catalytic capacity and stability, which would have a good application prospect.

3.2.3. Radical scavenging

After being stimulated by photons, the photogenerated carriers would react with water molecules and oxygen in the catalytic system to produce active groups [10,12]. Hydroxyl radicals (•OH), superoxide radicals ($•O_2^-$) and photogenerated holes (h^+) were all highly active, which would oxidize or reduce the substrates in photocatalytic reactions. In order to determine their importance, three experimental groups were parallel while a blank control group was set up. Three experimental groups were added with the same concentration of trapping agents which could inhibit different active groups. In detail, isopropanol (IPA), ethylenediamine tetraacetic acid (EDTA), and benzoquinone (BQ) were responsible for hydroxyl radicals (·OH), photogenerated holes (h^+) and superoxide radicals ($•O_2^-$) in the photocatalytic process [11,46]. The degradation efficiencies were investigated under the same conditions as the previous performance test. As shown in Fig. 10, the degradation rate of MA-4 decreased to different degrees after the addition of three different capture agents. It was verified that three aforesaid active groups contributed to the photocatalytic reaction. In these three scavenging experiments, the addition of EDTA had the greatest effect on the catalytic efficiency of MA-4, whose final degradation efficiency was 19.43%, indicating that h^+ played a key role in the photodegradation

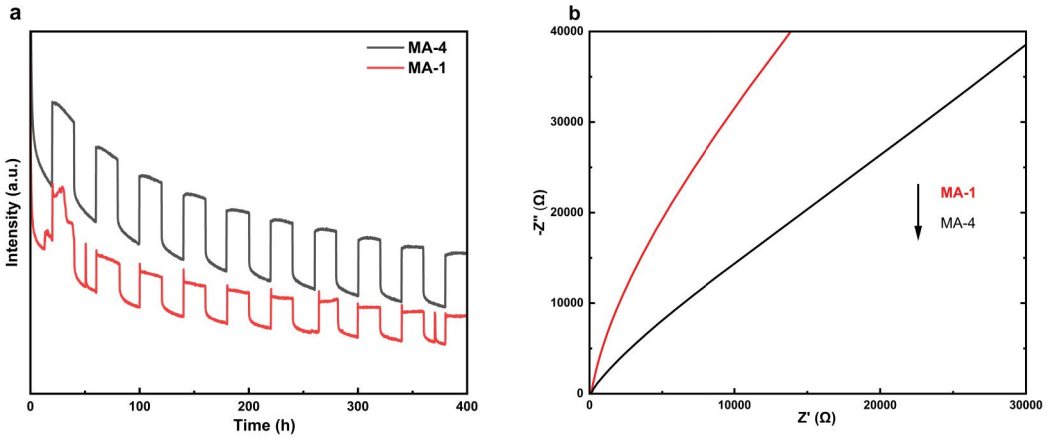

Fig. 7. (a) Photocurrent response densities and (b) EIS plots.

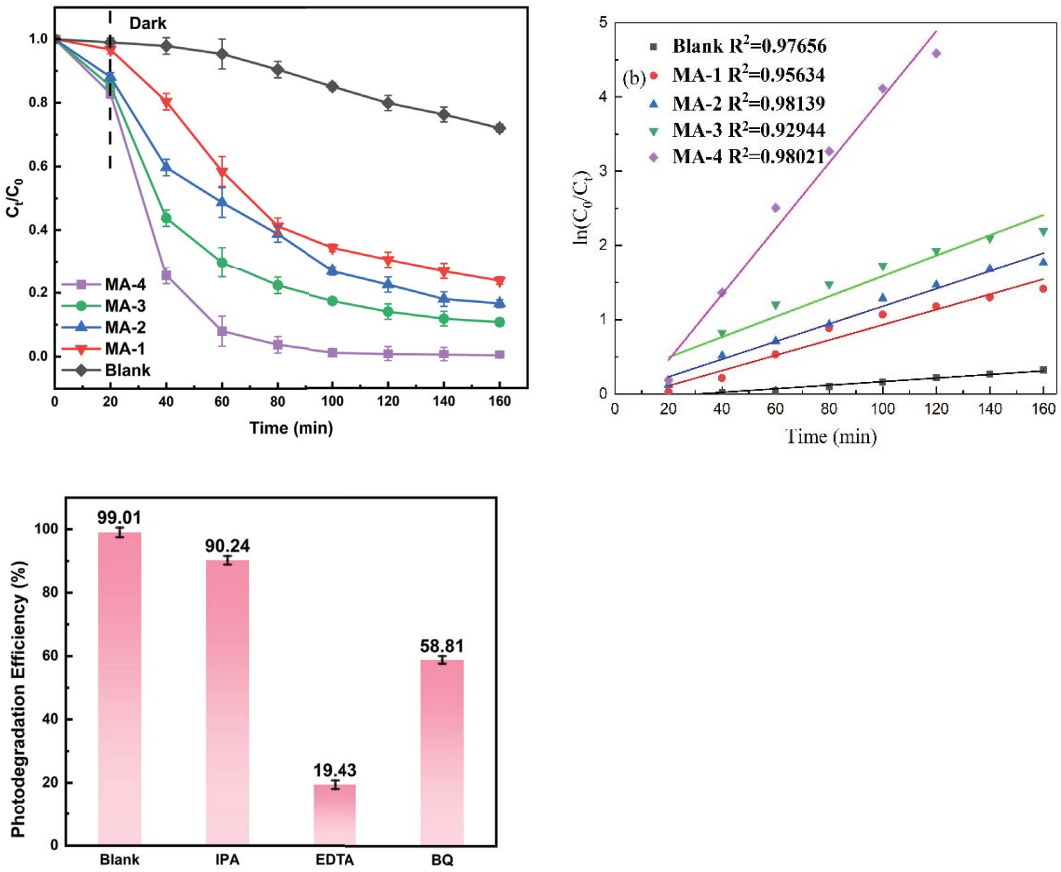

Fig. 8. (a) Photocatalytic degradation rate of TC over blank control group and MA series materials (25 mg catalysts, 15 ppm TC, 500 W mercury lamp), (b) the pseudo-first-order degradation kinetics for TC with different photocatalysts, used to estimate Langmuir–Hinshelwood coefficients, and (c) the rate constant *k* of TC with different photocatalysts.

Table 2
Comparison of photocatalytic degradation performance of tetracycline by catalyst photocatalysts reported in the literature with MA-4

Catalyst	Reaction time (min)	Degradation efficiency (%)	References
$BiVO_4/Ag/Cu_2O$	60	72.63	[34]
$RGO\text{-}Cu_2O/Fe_2O_3$	180	50.8	[35]
$Cu_2O/ZIF\text{-}8$	120	84.1	[36]
$Cu_2O/ZnTi\text{-}LDH$	120	71.6	[37]
BiOI/BiOBr	90	90	[38]
$CuInS_2/g\text{-}C_3N_4$	120	52.16	[39]
Bi_2WO_6/polyimide	120	65.1	[40]
Sludge-TiO_2	120	76.3	[41]
MA-4	180	99.34	This work

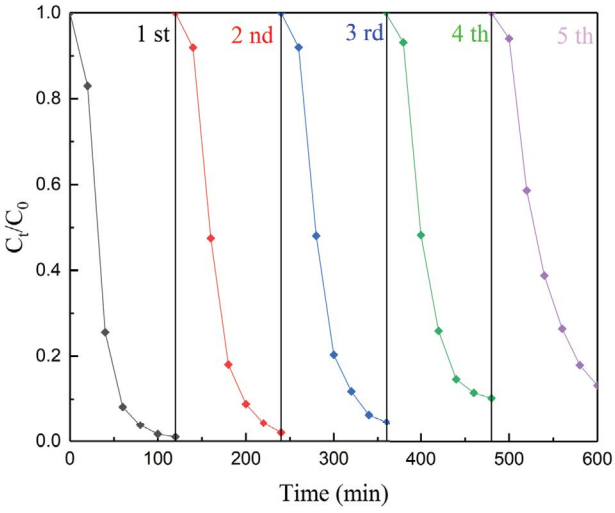

Fig. 9. Recycling photodegradation of TC with MA-4.

reaction. In addition, BQ had a strong inhibition effect on the system. MA-4 only degraded 58.81% of TC in the solution, demonstrating that $^{\bullet}O_2^-$ was an important radical involved in the reaction. In comparison, the photocatalytic activity of MA-4 decreased slightly with the addition of IPA (90.24%), confirming that $^{\bullet}OH$ had a little effect on the photocatalytic process. As a result, h^+ played a decisive role in the photocatalytic degradation of TC by MA-4, while the active groups $^{\bullet}O_2^-$ and $^{\bullet}OH$ also had a certain influence on the photoreaction.

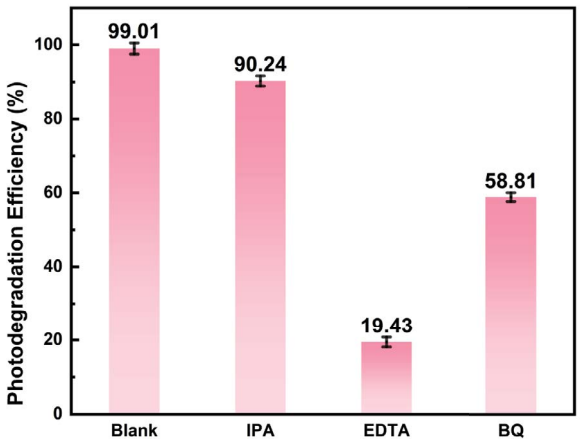

Fig. 10. Degradation efficiency of MA-4 with different capture agents (15 ppm TC, 25 mg MA-4, 500 W mercury lamp).

3.2.4. Photocatalytic mechanism of MgAl-LDH

In order to determine the energy band structure, the valence band (VB) of the photocatalyst could be obtained by an XPS valence-band spectrum. As Fig. 11 shows, the VB of MA-4 was obtained as 2.60 eV by linear extrapolation [47].

In addition, the conduction band (CB) potential of MA-4 could be determined by Eq. (2) [48–51].

$$E_{CB} = E_{VB} - E_g \quad (2)$$

where E_{CB} and E_{VB} represented the potentials of conduction band and valence band. E_g was the bandgap width. Based on the results of UV-Vis DRS (Fig. 5), the E_g value of 2D MgAl-LDH nanosheets was 3.90 eV. Thus, the CB of MA-4 could be calculated as –1.30 eV. According to the values of CB and VB, the possible mechanism of MA-4 photodegradation of TC could be proposed.

Based on the results of the radical scavenging test, h^+, $^{\bullet}OH$, and $^{\bullet}O_2^-$ had strong activity during the photodegradation process, particularly h^+ and $^{\bullet}O_2^-$. Photogenerated carriers were produced on the surface of MA-4 under light irradiation. Since the CB edge of the 2D MgAl-LDH (–1.30 eV) was more negative than E_0 ($O_2/^{\bullet}O_2^-$) (–0.33 eV vs. NHE), O_2 could be reduced to $^{\bullet}O_2^-$ by the photoelectrons on the material. Meanwhile, H_2O could be oxidized to $^{\bullet}OH$ on the LDH because the VB edge (2.60 eV) was more positive than E_0 ($H_2O/^{\bullet}OH$) (2.40 eV vs. NHE) [44–46,52,53]. In this way, as shown in Fig. 12, the band structure of the catalyst itself could support this redox process. Then, TC interacted with active radicals to form harmless molecules. Furthermore, the photodegradation process could be described by Eqs. (3)–(8).

$$\text{Photocatalyst} + hv \rightarrow e_{CB}^- + h_{VB}^+ \quad (3)$$

$$e_{CB}^- + O_2 \rightarrow {}^{\bullet}O_2^- \quad (4)$$

$$h_{VB}^+ + H_2O \rightarrow {}^{\bullet}OH + H^+ \quad (5)$$

$$h_{VB}^+ + TC \rightarrow \text{Degradation products} \quad (6)$$

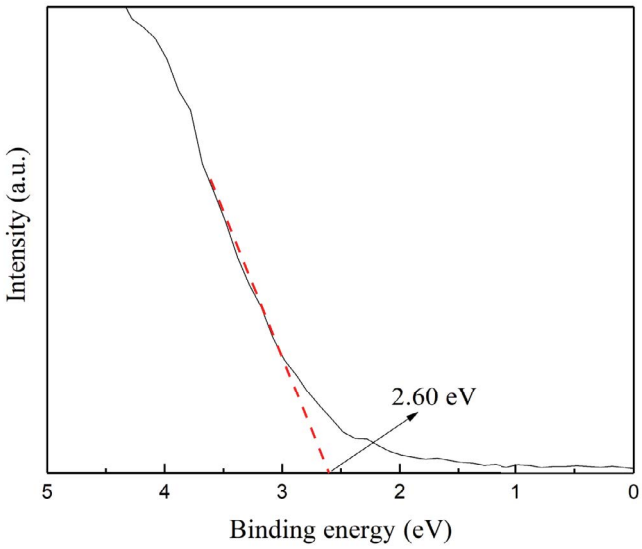

Fig. 11. Valence band spectrum of MA-4.

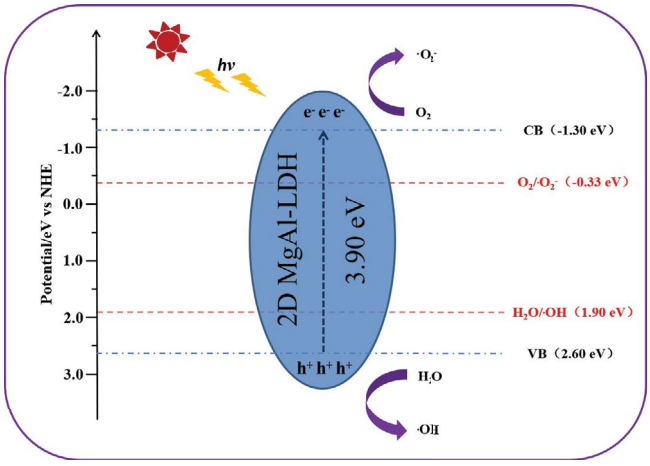

Fig. 12. Photocatalytic reaction mechanism of 2D MgAl-LDH for the degradation of TC.

$$^{\bullet}O_2^- + TC \rightarrow \text{Degradation products} \quad (7)$$

$$^{\bullet}OH + TC \rightarrow \text{Degradation products} \quad (8)$$

4. Conclusion

In summary, 2D MgAl-LDH nanosheets were successfully prepared via a simple hydrothermal method. Based on various characterization analyses, MA-4 prepared by 30% H_2O_2 as a stripping agent was an ultrathin nanosheet with an ideal sheet structure, large specific surface area, strong adsorption performance, narrow bandwidth, and wide spectral response region. In addition, the large specific surface area resulted in more active sites. Thus, 2D MgAl-LDH had the optimal photodegradation efficiency (99.34%) among all the samples. Furthermore, its degradation activity still remained higher than 85% after five cycles. Meanwhile, through the analysis of active radicals and the band structure of the photocatalyst,

the proposed mechanism could provide useful information for different application fields. This work not only suggests that 2D MgAl-LDH is a photocatalyst with practical application prospects but also provides new ideas for the preparation and application of two-dimensional materials.

Acknowledgment

The authors would like to thank the National Natural Science Foundation of China (Grant No. 21776319).

References

[1] Y.Z. Kuang, X.Y. Guo, J.R. Hu, S. Li, R.J. Zhang, Q. Gao, X. Yang, Q. Chen, W.L. Sun, Occurrence and risks of antibiotics in an Urban River in Northeastern Tibetan Plateau, Sci. Rep., 10 (2020) 20054, doi: 10.1038/s41598-020-77152-5.
[2] J.L. Wang, S.Z. Wang, Microbial degradation of sulfamethoxazole in the environment, Appl. Microbiol. Biotechnol., 102 (2018) 3573–3582.
[3] H.X. Wang, N. Wang, B. Wang, Q. Zhao, H. Fang, C.W. Fu, C.X. Tang, F. Jiang, Y. Zhou, Y. Chen, Q.W. Jiang, Antibiotics in drinking water in Shanghai and their contribution to antibiotic exposure of school children, Environ. Sci. Technol., 50 (2016) 2692–2699.
[4] R. Daghrir, P. Drogui, Tetracycline antibiotics in the environment: a review, Environ. Chem. Lett., 11 (2013) 209–227.
[5] H.P. Gao, Y.G. Wang, M.A. Afolabi, D.Q. Xiao, Y.S. Chen, Incorporation of cellulose nanocrystals into graphene oxide membranes for efficient antibiotic removal at high nutrient recovery, ACS Appl. Mater. Interfaces, 13 (2021) 14102–14111.
[6] X.H. Huang, J. Tian, Y.W. Li, X.L. Yin, W. Wu, Preparation of a three-dimensional porous graphene oxide–kaolinite–poly(vinyl alcohol) composite for efficient adsorption and removal of ciprofloxacin, Langmuir, 36 (2020) 10895–10904.
[7] A. Jaén-Gil, M.J. Farré, A. Sànchez-Melsió, A. Serra-Compte, D. Barceló, S. Rodríguez-Mozaz, Effect-based identification of hazardous antibiotic transformation products after water chlorination, Environ. Sci. Technol., 54 (2020) 9062–9073.
[8] K. Fischer, M. Majewsky, Co-metabolic degradation of organic wastewater micropollutants by activated sludge and sludge-inherent microorganisms, Appl. Microbiol. Biotechnol., 98 (2014) 6583–6597.
[9] N. Talreja, M. Ashfaq, D. Chauhan, A.C. Mera, C.A. Rodríguez, Strategic doping approach of the Fe–BiOI microstructure: an improved photodegradation efficiency of tetracycline, ACS Omega, 6 (2021) 1575–1583.
[10] R. Dhanabal, S. Velmathi, A.C. Bose, Fabrication of RuO_2-Ag_3PO_4 heterostructure nanocomposites: investigations of band alignment on the enhanced visible light photocatalytic activity, J. Hazard. Mater., 344 (2018) 865–874.
[11] Y.K. Wang, S. Zhou, G.Q. Zhao, C.F. Li, L.K. Liu, F.P. Jiao, Fabrication of $SnWO_4$/ZnFe-layered double hydroxide composites with enhanced photocatalytic degradation of methyl orange, J. Mater. Sci.: Mater. Electron., 31 (2020) 12269–12281.
[12] R.Q. Gang, L. Xu, Y. Xia, L.B. Zhang, S.X. Wang, R. Li, Facile one-step production of 2D/2D ZnO/rGO nanocomposites under microwave irradiation for photocatalytic removal of tetracycline, ACS Omega, 6 (2021) 3831–3839.
[13] X.F. Tan, S.B. Liu, Y.G. Liu, Y.L. Gu, G.M. Zeng, X.X. Cai, Z.L. Yan, C.P. Yang, X.J. Hu, B. Chen, One-pot synthesis of carbon supported calcined-Mg/Al layered double hydroxides for antibiotic removal by slow pyrolysis of biomass waste, Sci. Rep., 6 (2016) 39691, doi: 10.1038/srep39691.
[14] Y.H. Zheng, C.Q. Chen, Y.Y. Zhan, X.Y. Lin, Q. Zheng, K.M. Wei, J.F. Zhu, Y.J. Zhu, Luminescence and photocatalytic activity of ZnO nanocrystals: correlation between structure and property, Inorg. Chem., 46 (2007) 6675–6682.
[15] M. Bouslama, M.C. Amamra, Z. Jia, M. Ben Amar, K. Chhor, O. Brinza, M. Abderrabba, J.L. Vignes, A. Kanaev, Nanoparticulate TiO_2–Al_2O_3 photocatalytic media: effect of particle size and polymorphism on photocatalytic activity, ACS Catal., 2 (2012) 1884–1892.
[16] P. Li, H.C. Zeng, Immobilization of metal-organic framework nanocrystals for advanced design of supported nanocatalysts, ACS Appl. Mater. Interfaces, 8 (2016) 29551–29564.
[17] G.Q. Zhao, L.K. Liu, C.F. Li, J.G. Yu, F.P. Jiao, Synthesis, characterization and enhanced visible light photocatalytic activity of Bi_2WO_6/Ni-Al layered double hydroxide composites, J. Mater. Sci.: Mater. Electron., 29 (2018) 14008–14021.
[18] G.L. Fan, F. Li, D.G. Evans, X. Duan, Catalytic applications of layered double hydroxides: recent advances and perspectives, Chem. Soc. Rev., 43 (2014) 7040–7066.
[19] C.Y. Yang, T.H. Zhu, J. Wang, S.H. Chen, W.Y. Li, Synthesis and characterization offlurbiprofen axetil-loaded electrospun MgAl-LDHs/poly(lacticco-glycolic acid) composite nanofibers, RSC Adv., 5 (2015) 69423–69429.
[20] C.P. Chen, J.C. Buffet, D. O'Hare, Surface modification of aqueous miscible organic layered double hydroxides (AMO-LDHs), Dalton Trans., 49 (2020) 8498–8503.
[21] S. Iguchi, Y. Hasegawa, K. Teramura, S. Kidera, S. Kikkawa, S. Hosokawa, H. Asakura, T. Tanaka, Drastic improvement in the photocatalytic activity of Ga_2O_3 modified with Mg-Al layered double hydroxide for the conversion of CO_2 in water, Sustainable Energy Fuels, 1 (2017) 1740–1747.
[22] T.T. Kong, J. Huang, X.G. Jia, W.Z. Wang, Y. Zhou, Synthesis and optimization of Ti/Li/Al ternary layered double hydroxides for efficient photocatalytic reduction of CO_2 to CH_4, Sci. Rep., 9 (2019) 5659, doi: 10.1038/s41598-019-41979-4.
[23] K.L. Huang, C.H. Li, H.Z. Li, G.M. Ren, L. Wang, W.T. Wang, X.C. Meng, Photocatalytic applications of two-dimensional Ti_3C_2 MXenes: a review, ACS Appl. Nano Mater., 3 (2020) 9581–9603.
[24] L. Cheng, X. Li, H.W. Zhang, Q.J. Xiang, 2D transition metal MXene-based photocatalysts for solar fuel generation, J. Phys. Chem. Lett., 10 (2019) 3488–3494.
[25] P. Vols, S. Hilbert, B. Storr, N. Bette, A. Lissner, J. Seidel, F. Mertens, Methanation of CO_2 and CO by (Ni, Mg, Al)-hydrotalcite-derived and related catalysts with varied magnesium and aluminum oxide contents, Ind. Eng. Chem. Res., 60 (2021) 5114–5123.
[26] N. Blanch-Raga, A.E. Palomares, J. Martínez-Triguero, G. Fetter, P. Bosch, Cu mixed oxides based on hydrotalcite-like compounds for the oxidation of trichloroethylene, Ind. Eng. Chem. Res., 52 (2013) 15772–15779.
[27] H. Mitta, P.K. Seelam, K.V.R. Chary, S. Mutyala, R. Boddula, Inamuddin, A.M. Asiri, Efficient vapor-phase selective hydrogenolysis of bio-levulinic acid to γ-valerolactone using Cu supported on hydrotalcite catalysts, Global Challenges, 2 (2018) 1800028, doi: 10.1002/gch2.201800028.
[28] N. Zhang, C. Chen, Z.W. Mei, X.H. Liu, X.L. Qu, Y.X. Li, S.Q. Li, W.H. Qi, Y.J. Zhang, J.H. Ye, V.A.L. Roy, R.Z. Ma, Monoclinic tungsten oxide with {100} facet orientation and tuned electronic band structure for enhanced photocatalytic oxidations, ACS Appl. Mater. Interfaces, 8 (2016) 10367–10374.
[29] J.D. Xiao, Y.B. Xie, F. Nawaz, Y.X. Wang, P.H. Du, H.B. Cao, Dramatic coupling of visible light with ozone on honeycomb-like porous g-C_3N_4 towards superior oxidation of water pollutants, Appl. Catal., B, 183 (2016) 417–425.
[30] Y.X. Yan, Q. Liu, J. Wang, J. Wei, Z. Gao, T. Mann, Z.S. Li, Y. He, M.L. Zhang, L.H. Liu, Single-step synthesis of layered double hydroxides ultrathin nanosheets, J. Colloid Interface Sci., 371 (2012) 15–19.
[31] X.Y. Li, J.J. Xue, S.S. Mal, P. Xu, C.J. Huang, M.X. Wang, Synthesis of MgAl LDH/acidified g-C_3N_4 heterojunction photocatalyst for improved tetracycline hydrochloride degradation activity, NANO: Brief Rep. Rev., 14 (2019) 1950066.
[32] G. Zhang, D. Yang, E. Sacher, Structure and morphology of Co nanoparticles deposited onto highly oriented pyrolytic graphite, J. Phys. Chem. C, 111 (2007) 17200–17205.
[33] D.J. Liang, W.B. Yue, G.B. Sun, D. Zheng, K. Ooi, X.J. Yang, Synthesis of unilamellar MgAl-LDH nanosheets and stacking in aqueous solution, Langmuir, 31 (2015) 12464–12471.

[34] H. Shen, M. Wang, X. Zhang, D. Li, G. Liu, W. Shi, 2D/2D/3D architecture Z-scheme system for simultaneous H_2 generation and antibiotic degradation, Fuel, 280 (2020) 118618, doi: 10.1016/j.fuel.2020.118618.
[35] H. Shen, G. Liu, X. Yan, J. Jiang, Y. Hong, M. Yan, B. Mao, D. Li, W. Fan, W. Shi, All-solid-state z-scheme system of RGO-Cu_2O/Fe_2O_3 for simultaneous hydrogen production and tetracycline degradation, Mater. Today Energy, 5 (2017) 312–319.
[36] Y. Zhou, S. Feng, X. Duan, W. Wu, Z. Ye, X. Dai, Y. Wang, X. Cao, Stable self-assembly Cu_2O/ZIF-8 heterojunction as efficient visible light responsive photocatalyst for tetracycline degradation and mechanism insight, J. Solid State Chem., 305 (2022) 122628, doi: 10.1016/j.jssc.2021.122628.
[37] J. Xiong, H.Y. Zeng, J.F. Peng, L.H. Wang, D.Y. Peng, F.Y. Liu, S. Xu, Z.L. Yang, Fabrication of Cu_2O/ZnTi-LDH p-n heterostructure by grafting Cu_2O nps onto the LDH host layers from Cu-doped ZnTi-LDH and insight into the photocatalytic mechanism, Composites, Part B, 250 (2023) 110447, doi: 10.1016/j.compositesb.2022.110447.
[38] Q. Ni, X. Ke, W. Qian, Z. Yan, J. Luan, W. Liu, Insight into tetracycline photocatalytic degradation mechanism in a wide pH range on BiOI/BiOBr: coupling DFT/QSAR simulations with experiments, Appl. Catal., B, 340 (2024) 123226, doi: 10.1016/j.apcatb.2023.123226.
[39] J. Zhang, Y. Zhao, K. Qi, S.-y. Liu, CuInS2 quantum-dot-modified g-C_3N_4 S-scheme heterojunction photocatalyst for hydrogen production and tetracycline degradation, J. Mater. Sci. Technol., 172 (2024) 145–155.
[40] X. Gao, J. Niu, Y. Wang, Y. Ji, Y. Zhang, Solar photocatalytic abatement of tetracycline over phosphate oxoanion decorated Bi_2WO_6/polyimide composites, J. Hazard. Mater., 403 (2021) 123860, doi: 10.1016/j.jhazmat.2020.123860.
[41] X. Zhu, W. Yuan, M. Lang, G. Zhen, X. Zhang, X. Lu, Novel methods of sewage sludge utilization for photocatalytic degradation of tetracycline-containing wastewater, Fuel, 252 (2019) 148–156.
[42] J.S. Valente, M.S. Cantu, J.G.H. Cortez, R. Montiel, X. Bokhimi, E. Lopez-Salinas, Preparation and characterization of sol–gel MgAl hydrotalcites with nanocapsular morphology, J. Phys. Chem. C, 111 (2007) 642–651.
[43] F.S. Li, L. Jin, J.B. Han, M. Wei, C.J. Li, Synthesis and controlled release properties of prednisone intercalated Mg-Al layered double hydroxide composite, Ind. Eng. Chem. Res., 48 (2009) 642–651.
[44] F. Hasanvandian, M. Moradi, S.A. Samani, B. Kakavandi, S.R. Setayesh, M. Noorisepehr, Effective promotion of g-C_3N_4 photocatalytic performance via surface oxygen vacancy and coupling with bismuth-based semiconductors towards antibiotics degradation, Chemosphere, 287 (2022) 132273, doi: 10.1016/j.chemosphere.2021.132273.
[45] M. Ahmadi, M. Moslemzadeh, A. Naderi, M.Z. Salmasi, M. Harati, R.R. Kalantary, B. Kakavandi, Intensified photodegradation of nitrobenzene using ZnO-anchored spinel cobalt ferrite: environmental application, mechanism, and degradation pathway, J. Water Process. Eng., 49 (2022) 103064, doi: 10.1016/j.jwpe.2022.103064.
[46] B. Zhang, R.T. Hu, D.J. Sun, T. Wu, Y.J. li, Fabrication of magnetite-graphene oxide/MgAl-layered double hydroxide composites for efficient removal of emulsified oils from various oil-in-water emulsions, J. Chem. Eng. Data, 63 (2018) 4689–4702.
[47] Y.M.H. Zhou, L. Shuai, X.Y. Jiang, F.P. Jiao, J.G. Yu, Visible-light-driven photocatalytic properties of layered double hydroxide supported-Bi_2O_3 modified by Pd(II) for methylene blue, Adv. Powder Technol., 26 (2015) 439–447.
[48] G.Q. Zhao, C.F. Li, X. Wu, J.G. Yu, X.Y. Jiang, W.J.H. Hu, F.P. Jiao, Reduced graphene oxide modified NiFe-calcinated layered double hydroxides for enhanced photocatalytic removal of methylene blue, Appl. Surf. Sci., 434 (2018) 251–259.
[49] G.H. Zhang, W.S. Guan, H. Shen, X. Zhang, W.Q. Fan, C.Y. Lu, H.Y. Bai, L.S. Xiao, W. Gu, W.D. Shi, Organic additives-free hydrothermal synthesis and visible-light-driven photodegradation of tetracycline of WO_3 nanosheets, Ind. Eng. Chem. Res., 53 (2014) 5443–5450.
[50] B. Carlson, K. Leschkies, E.S. Aydil, B. Carlson, X.Y. Zhu, Valence band alignment at cadmium selenide quantum dot and zinc oxide (1010) interfaces, J. Phys. Chem. C, 112 (2008) 8419–8423.
[51] M. Moradi, B. Kakavandi, A. Bahadoran, S. Giannakis, E. Dehghanifard, Intensification of persulfate-mediated elimination of bisphenol A by a spinel cobalt ferrite-anchored g-C_3N_4 S-scheme photocatalyst: catalytic synergies and mechanistic interpretation, Sep. Purif. Technol., 120 (2022) 120313, doi: 10.1016/j.seppur.2021.120313.
[52] W.T. Sun, S. Meng, S.J. Zhang, X.Z. Zheng, X.J. Ye, X.L. Fu, S.F. Chen, Insight into the transfer mechanisms of photogenerated carriers for heterojunction photocatalysts with the analogous positions of valence band and conduction band: a case study of ZnO/TiO_2, J. Phys. Chem. C, 122 (2018) 15409–15420.
[53] M. Mousavi, A. Habibi-Yangjeh, S.R. Pouran, Review on magnetically separable graphitic carbon nitride-based nanocomposites as promising visible-light-driven photocatalysts, J. Mater. Sci., 29 (2018) 1719–1747.